Title

Numerical Modelling of High-speed Silicon MRM/MRR

ISBN

9798186386759

Author

Kim, Aaron

Publication Date

2026-06-16

Peer reviewed|Thesis/dissertation

UNIVERSITY OF CALIFORNIA

Santa Barbara

Numerical Modelling of High-speed Silicon MRM/MRR

A Thesis submitted in partial satisfaction of the

requirements for the degree Master of Science

in Electrical and Computer Engineering

by

Aaron Kim

Committee in charge:

Professor Clint L. Schow, Chair

Professor Daniel J. Blumenthal

Professor James F. Buckwalter

Professor Galan Moody

June 2026

The thesis of Aaron Kim is approved.

Daniel J. Blumenthal

James F. Buckwalter

Galan Moody

Clint L. Schow, Committee Chair

June 2026

Numerical Modelling of High-speed Silicon MRM/MRR

by

Aaron Kim

ACKNOWLEDGEMENTS

I express my sincere appreciation to my advisor, Professor Schow, for his technical guidance and support throughout my research in the Department of Electrical and Computer Engineering at UC Santa Barbara. I extend my gratitude to my thesis committee members for their constructive feedback, and dedicated time in evaluating this work. I especially thank my senior PhD student, Ankit Kumar, for his mentorship and help in constructing the project and research direction in the very beginning. Lastly, I am deeply grateful to my family for their continuous encouragement and financial support throughout the duration of my Master of Science degree program.

ABSTRACT

Numerical Modelling of High-speed Silicon MRM/MRR

by

Aaron Kim

The rapid scaling of artificial intelligence computation has exposed electrical interconnects as a critical bottleneck in modern data centers, driving the industry toward silicon photonics and high-speed wavelength division multiplexing links. As networking standards have evolved to demand >100G per lane, the architectural paradigm has shifted from massively parallel, moderate-speed microring arrays to fewer, high-baud-rate channels. Despite this aggressive scaling, existing literature remains heavily focused on isolated device-level demonstrations, lacking systematic parametric studies that connect fundamental microring geometry to system-level Bit Error Rate performance. To address this gap, this thesis presents a comprehensive, multi-physics numerical modeling framework for high-speed Silicon Microring Modulators (MRM) and Microring Resonators (MRR) on a 160 nm standard platform. Utilizing an end-to-end simulation flow (MODE, FDTD, HEAT, CHARGE, and INTERCONNECT), the fundamental trade-offs between optical bandwidth, insertion loss, and extinction ratio are systematically evaluated. For the receiver MRR, transient step-response characterization reveals that the optical cavity behaves as alow-pass filter, dictating that wider optical bandwidths are strictly required to mitigate Inter-Symbol Interference at speeds exceeding 100 Gbps. For the transmitter MRM, realistic PN junction parameters are

benchmarked from literature to evaluate the complex trade-off between optical modulation amplitude and cavity bandwidth. Through rigorous multi-dimensional parameter sweeps of active doping concentrations and drive voltages, an optimal operating regime is identified. The optimized silicon MRM successfully demonstrates a 100 Gbps transmission rate satisfying the concatenated forward error correction limit at a 2 V peak-to-peak drive voltage. Ultimately, this thesis establishes a robust device-to-system co-simulation methodology while revealing the fundamental, rigid speed limits of standard silicon-on-insulator microrings, highlighting the necessity for advanced junction engineering and the eventual transition to highly efficient electro-optic materials.

TABLE OF CONTENTS

LIST OF FIGURES

I. Introduction

A. Background and Motivation

The rapid scaling of artificial intelligence (AI) training and hardware computation has led to an exponential increase in the demand for data transfer capabilities [1]. To address this limitation, Silicon Photonics has been widely adopted as a next-generation interconnect solution for AI data centers [2-3]. Specifically, Silicon Micro-Ring Modulator (MRM) and Micro-Ring Resonator (MRR) Wavelength Division Multiplexing (WDM) links offer compelling advantages. These include strict CMOS compatibility, an exceptionally small device footprint, and the inherent capability to multiplex multiple carrier wavelengths $(\lambda_1, \lambda_2, \lambda_2, , ,)$ onto a single waveguide. In a typical MRM-MRR WDM architecture as shown in Figure.1, an external laser provides the continuous-wave optical carriers, the transmitter (Tx) MRMs selectively modulate the data onto specific wavelengths, and the receiver (Rx) MRRs selectively filter and route the modulated signals to photodetectors.

Figure.1 Schematic of a single-channel silicon MRM-MRR WDM link and flow chart showing modulation and demodulation

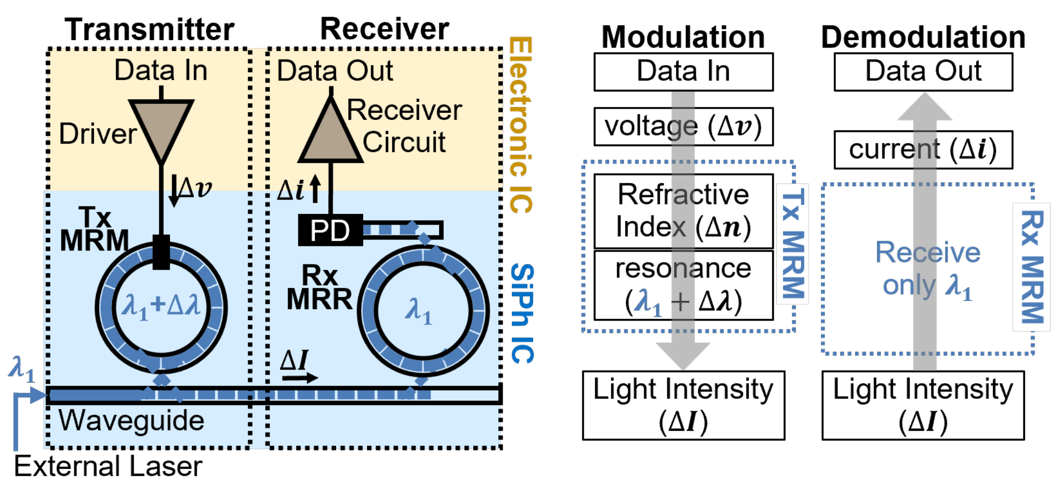

Early approaches to scaling the bandwidth of silicon photonic links relied heavily on a high number of moderate-speed modulators. To boost the aggregate bandwidth, previous attemps simply increased the number of MRM-MRR pairs along the waveguide rather than improving the per-lane data rate [4-7]. While this approach provided a temporary solution, it lacked long-term scalability. Multiplying the number of optical ring pairs proportionally increases the number of required electronic driver and receiver circuits, leading to a highly complex and congested electronic-photonic co-design. Furthermore, it significantly exacerbates the static power consumption of the system, as each individual ring requires dedicated thermal tuning heaters to maintain resonance alignment against thermal crosstalk and fabrication variations. Furthermore, moderate-speed devices do not meet the stringent power and footprint demands of modern high-performance AI interconnects.

Recently, industry has shifted toward architecture utilizing a lower number of high-speed modulators per lane. This transition is clearly visible in the IEEE Ethernet standards, such as IEEE 802.3df and the ongoing IEEE 802.3dj, which mandate scaling bitrates to 100G, 200G, and 400G per lane [8]. Operating at these high baud rates (e.g., 224 Gbps PAM4 for 200G/lane) necessitates strict adherence to specific Forward Error Correction (FEC) schemes to ensure data integrity. The selection of FEC schemes is dictated by the target post-FEC Bit Error Rate (BER), typically 1×10^{-15}, which defines the maximum allowable pre-FEC BER threshold. For instance, achieving a 224 Gbps link under a concatenated KP4+Hamming (128,120) scheme requires a pre-FEC BER of less than 4.85×10^{-3} [9-11].

Table.1. Comparison table of high-speed (> 100 Gbps) MRM literatures

Ref	*radius [um]*	*Q*	*Modeff [pm/V]*	*BW [GHz]*	*Bitrate [Gbps]*	*FEC*
[14] HK Poly, CAS 2025		4500	17	25	100	HD
[15] HUST 2022	9	7000	23 38	42	100 50 (NRZ)	
[16] CAS 2025	6	3700	22.5	60	106 128 (NRZ)	
[17] Intel 2020	10	3300	30	55 (series peaking Inductor)	112	
[18] Intel 2019	10		0.52 Vcm	50	128	
[19] HUST 2025	9		32	35-41		
[20] Shanghi, CAS 2024			27.5 31.5	39 34	140 120	
[21] Acacia Communications 2024	15	5000		42	144	HD
[22] Intel 2021	6	4200	26,33	77 (-3dB detuning) 63(-6),58(-9)	192 128(NRZ)	
[23] CUHK, HK Poly 2022	3	1050	0.94 Vcm	67	200 120(NRZ)	HD
[24] HUST 2025	8	5200 5000	33.5 24.3	67	200 128(NRZ)	SD
[25] Hewlett Packard Enterprise 2024	12	3700		48.3, 48.9 (MSB,LSB)	200	SD
[26] CUHK 2024	7.5	5100	0.56 Vcm		210 180(NRZ)	
[27] Wuhan-CICT 2022	8	4500	0.825Vcm	110 ($\Delta\lambda$=0.326nm) 52 ($\Delta\lambda$=0.115nm)	240(PAM8) 120(NRZ)	
[28] HIT, HKUST 2025	4.45 (L=28)	1900	18, (1.71 Vcm)	110 ($\Delta\lambda$=0.45nm) 86 ($\Delta\lambda$=0.3nm)	224	SD
[29] CAS 2025	6	2500	33	67 (-3dB detuning)	256	SD
[30] HKUST 2025	3 3.5	1170 1475	25 30	110 (detuning)	300 256 182(NRZ)	SD HD
[31] Fudan, Wuhan-CICT 2023	8	3300	0.8 Vcm	42.5 ($\Delta\lambda$=0.183nm)	302	Bi-GRU NN

Despite the rapid and aggresive industry shift toward >100G/lane interconnects, current academic and industrial research has largely remained focused on device-level demonstrations, as shown in Table.1. [14-31]. They lack broad, systematic parametric studies. Moreover, there is no work that comprehensively and systematically sweeps both MRM device parameters and link-level parameters simultaneously to explore their comprehensive impact on BER changes. To address this gap, this project aims to explore the design methodology and evaluate the performance of MRM/MRR operating at high speeds for WDM applications, with a primary focus on BER outcomes. By conducting systematic numerical modeling and design space exploration, this thesis establishes device-to-system simulation flows to better understand the high-speed design trade-offs of MRMs and MRRs. The findings of this parametric study establish a foundation for the rigid design of high-speed MRM/MRR WDM links, to be pursued in future work following this thesis.

B. Scope and Limitations

The primary scope of this thesis is restricted to the numerical modeling and design space exploration of high-speed silicon MRR and MRM. The research focuses on establishing robust device-to-system simulation flows to systematically evaluate high-speed design trade-offs and conduct rigorous BER analyses. All component-level and system-level simulations are strictly bound to a standard 160 nm Silicon-on-Insulator (SOI) platform. Details are in the next section.

To isolate the fundamental electro-optic performance and high-speed transient behaviors of the microring devices, several physical and systemic complexities are intentionally excluded from the modeling flow. Specifically, the numerical models assume ideal structural profiles and do not account for fabrication variations. While thermal properties are utilized to establish baseline resonant conditions, complex thermal crosstalk, temperature-induced instabilities, and explicit thermal heater design are not considered in this work. Furthermore, nonlinear optical bi-stability limits and overall system power consumption metrics are ignored during the performance evaluations. These exclusions ensure that the calculated performance ceilings and signal degradations are strictly attributed to the intrinsic high-speed electro-optic characteristics of the evaluated MRM and MRR designs.

C. Photonic Stacks and Waveguide Geometry

The baseline photonics platform for this numerical study is defined by a 160 nm SOI process. This specific structural thickness is selected for compatibility with the GlobalFoundries 45nm CMOS-compatible platform (GF45CLO) [32], which serves as the foundational reference for the PN junction parameter benchmarking utilized in later stages of this work [35-36]. The foundational optical stack consists of a 2 μm Buried Oxide (BOX) layer, a 2 μm top cladding (Clad) layer, and an Inter-Metal Dielectric (IMD) layer of approximately 4 μm. While explicit metal routing layers are intentionally omitted from all simulations, the 4 μm IMD thickness is sufficient to accommodate a standard back-end-of-line (BEOL) metal stack (e.g., M1, V1, M2, V2, and LB) [34-35]. Because the presence and specific configuration of the IMD primarily dictate the thermal dissipation characteristics rather than the core electro-optic performance, this assumption provides a valid baseline. The stack can be readily modified in future iterations if advanced thermal boundary effects require more rigorous investigation.

Regarding the active tuning components, a top-side metallic Titanium thermal heater is utilized in the simulation models. Although the reference GF45CLO platform typically employs integrated doped-silicon (silicide) heaters, explicit heater design, optimization, and rigorous thermal crosstalk analysis fall outside the defined scope of this thesis. The simplified Titanium heater provides a sufficient thermal boundary condition for modeling temperature-dependent resonance shifts.

For the core optical routing and resonant cavities, rib waveguides are exclusively utilized for all constructed MRMs and MRRs, rather than fully etched strip waveguides. The core waveguide width is fixed at 400 nm, while the slab thickness varies between 90 nm and 70 nm, and the ring radius is set to either 7.5 μm or 9 μm depending on the specific design iteration. The strategic selection of rib waveguides over strip waveguides is to lower the cavity Q-factor. By doing so, the baseline optical bandwidth of the resonators is inherently boosted, which is a critical architectural requirement for supporting the demanding baud rates of next-generation high-speed interconnects.

Figure.2 Schematic of photonic layers assumed in this project

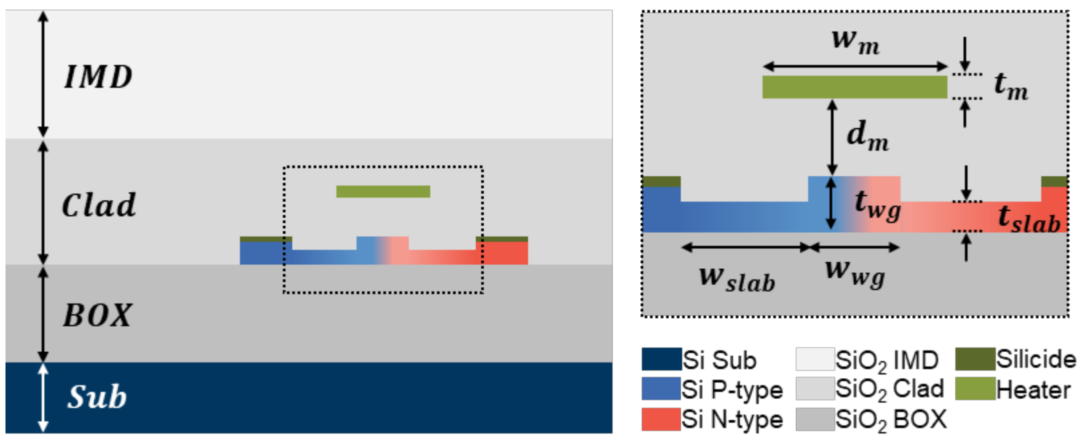

D. Preview of Thesis

This thesis is organized into three primary chapters to systematically establish the numerical modeling methodology and evaluate the system-level performance of high-speed silicon microring devices. The current chapter, Chapter I, establishes the primary background and motivation for this work, detailing the industry shift toward high-speed optical interconnects and defining the fundamental photonic stack and waveguide geometries that serve as the baseline for all subsequent simulations. Chapter II focuses entirely on the passive MRR acting as a Rx-side filter. It begins by introducing the governing analytical round-trip field model before detailing a comprehensive, multi-physics simulation flow utilizing the Lumerical software suite (MODE, FDTD, HEAT, and INTERCONNECT). The chapter systematically characterizes the MRR compound model through both steady-state transmission and transient step-response analyses, concluding with an evaluation of the overall system-level performance and BER. Finally, Chapter III transitions to the active transmitter, the MRM. Because the MRM relies on dynamic carrier dispersion, this chapter begins by benchmarking realistic fabrication-induced junction parameters to ensure simulation accuracy. It then investigates the critical trade-offs between average optical signal levels and Optical Modulation Amplitude requirements. By establishing a modified electro-optic simulation flow that accounts for internal RC delays and active cavity shifts, the chapter ultimately presents the definitive system-level MRM results, identifying the optimal parameters for maximizing high-speed data transmission.

II. Microring Resonator

A. Round Trip Model

A MRR operates as a highly wavelength-selective resonant system, characterized by sharp optical transmission peaks or dips at specific resonance wavelengths. The optical behavior of an MRR is fundamentally described by the round-trip field model [37-38]. In a standard add-drop configuration, light from a continuous-wave (CW) external laser enters the input port and partially couples into the circular ring waveguide. As the optical field circulates within the ring, it accumulates a phase shift and experiences propagation loss. After completing a round trip, the circulating field interferes with the newly coupled incoming light. Constructive interference at specific wavelengths results in optical resonance, which dictates the transmission responses at the pass (through) and drop ports. For the numerical modeling in this study, the round-trip model assumes an ideal CW laser input, lossless directional coupling (where the cross-coupling coefficient k and self-coupling coefficient r satisfy $r^2 + k^2 = 1$, and negligible back-reflection at the couplers.

Figure.3 Schematic of an add-drop resonator and power transmission spectrum

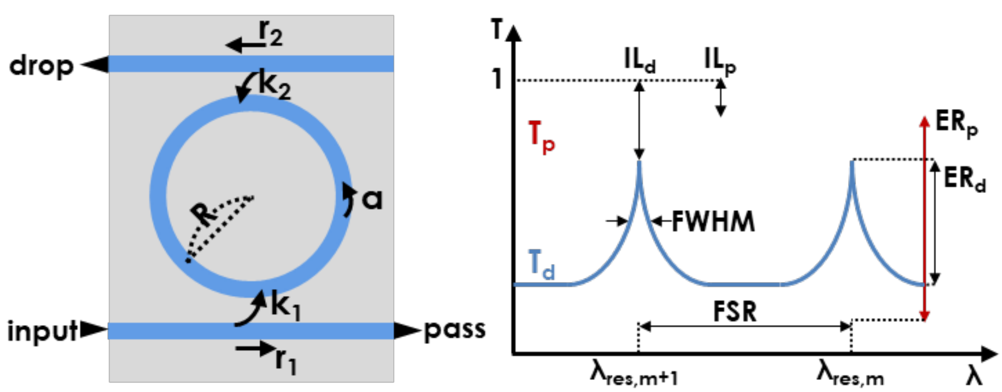

Figure.4 Calculated Characteristic Parameters. (left) Photon-lifetime limited bandwidth and (right) insertion loss and extinction ratio for drop-port as functions of the coupling coefficient for different round-trip loss coefficient where $\boldsymbol{r_1 = r_2 = r}$

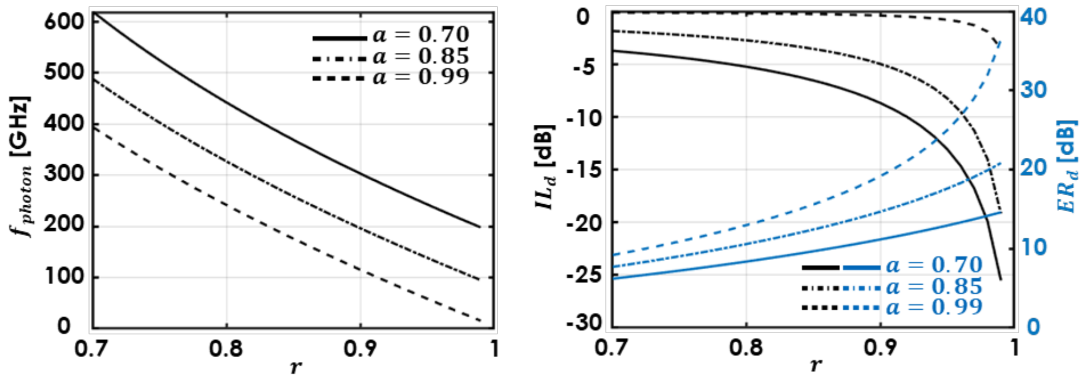

The steady-state optical performance of the MRR is quantified through several critical characteristic parameters derived from the round-trip model. The primary metric is the power transmission T, which must be analyzed for both the pass port T_p and the drop port T_d. The optical performance exactly at resonance is further characterized by the Insertion Loss (IL) and the Extinction Ratio (ER). Additionally, the spectral width of the resonance is defined by the Full Width at Half Maximum ($FWHM$), which strictly determines the photon lifetime and bandwidth f_{photon}, while the spectral spacing between adjacent resonant modes is defined as the Free Spectral Range (FSR). The governing equations for these characteristic parameters are detailed in the following tables.

Table.2. List of Round-trop Model Parameters

L	*circumference*
α	*round-trip loss*
a	*single-pass transmission*
r	*self-coupling coefficient*
k	*cross-coupling coefficient*
n_{eff}	*effective index*

n_g	*group index*
λ_{eff}	*resonance wavelength*
λ	*wavelength*
β	*propagation constant*
$\emptyset$	*single-pass phase shift*
FSR	*free-spectral range*
$FWHM$	*full-width half-maximum*
IL	*insertion loss*
ER	*extinction ratio*
T	*power transmission*

Table.3. Equations of Round-trip Model Parameters

$a = e^{-\alpha L} = e^{-\alpha 2\pi R}$	${r_{1,2}}^2 + {k_{1,2}}^2 = 1$
$\emptyset = \beta L = (2\pi n_{eff}/\lambda)L$	$FSR = {\lambda_{res}}^2/n_g L$
$\lambda_{res,m} = n_{eff}L/m$ $m = (0,1,2,,,)$	$FWHM = \frac{(1 - r_1 r_2 a){\lambda_{res}}^2}{\pi n_g L\sqrt{r_1 r_2 a}}$
$IL_p = \frac{(ar_2 + r_1)^2}{(1 + r_1 r_2 a)^2}$	$IL_d = \frac{(1 - {r_1}^2)(1 - {r_2}^2)a}{(1 - r_1 r_2 a)^2}$
$ER_p = \frac{(ar_2 + r_1)^2}{(ar_2 - r_1)^2}\frac{(1 - r_1 r_2 a)^2}{(1 + r_1 r_2 a)^2}$	$ER_d = \frac{(1 + r_1 r_2 a)^2}{(1 - r_1 r_2 a)^2}$
$T_p = \frac{I_{through}}{I_{input}} = \frac{{r_2}^2 a^2 - 2r_1 r_2 a\cos(\emptyset) + {r_1}^2}{1 - 2r_1 r_2 a\cos(\emptyset) + (r_1 r_2 a)^2}$	
$T_d = \frac{I_{drop}}{I_{input}} = \frac{(1 - {r_1}^2)(1 - {r_2}^2)a}{1 - 2r_1 r_2 a\cos(\emptyset) + (r_1 r_2 a)^2}$	
$f_{photon} = \frac{f_{res}}{Q} = FWHM\frac{c}{{\lambda_{res}}^2}$	

Analyzing these characteristic equations reveals inherent physical trade-offs in MRR design. Assuming a target O-band resonance wavelength λ_{res} of 1.3 μm, a group index n_g of 3.9, and a ring radius R of 7.5 μm, the relationship between the physical device parameters and the optical response can be established. The two primary variables governing the resonant response are the round-trip transmission factor a (which is inversely related to the waveguide propagation loss) and the self-coupling coefficient r. There are clear competing trends as these variables change. As a increases (indicating a lower round-trip loss), the photon lifetime limited bandwidth or optical bandwidth (f_{photon}) decreases, the drop-port insertion loss (IL_d) decreases, and the drop-port extinction ratio (ER_d) increases. Similarly, increasing the coupling coefficient r, which means weaker coupling from the bus waveguide to the ring, also reduces f_{photon}. On the other hand, a higher r negatively impacts by increasing IL_d and ER_d.

Because of these trade-offs, it is analytically impractical to determine a single "optimal" operating point solely through device-level optical equations. Optimizing for high-speed operation inevitably penalizes other metrics. Ultimately, the true metric of system performance in a WDM link is the BER, which accounts for both the device-level electro-optic responses and link-level noise penalties simultaneously. To systematically find the optimal point through BER analysis, the physical geometry of the MRR is varied to map out the design space. Three distinct MRR designs are evaluated, strategically chosen to achieve different baseline round-trip transmission values (a ranging from approximately 0.90 to 0.99):

- MRR#1: a 90 nm slab thickness and a 7.5 μm radius, $a \approx 0.9$.
- MRR#2: a 90 nm slab thickness and a 9.0 μm radius, $a \approx 0.95$.
- MRR#3: a 70 nm slab thickness and a 9.0 μm radius, $a \approx 0.99$.

For each of these three designs, the waveguide coupling gap is parametrically swept from 150 to 350 nm. This sweep effectively varies r, allowing for a comprehensive simulation of device states and the subsequent evaluation of BER across a wide high-speed design space.

B. Simulation Flow

To accurately capture the multi-physics behavior of the MRR and evaluate its performance at the system level, a comprehensive simulation flow is established, referring to [39,40]. This flow integrates component-level solvers with system-level architectures to systematically calculate the transmission spectrum analytically and construct an MRR compound model within Lumerical INTERCONNECT. As illustrated in the simulation flow, the process begins with establishing the thermal boundaries. A heat solver (HEAT) generates a temperature profile, which is then fed into an eigenmode solver (MODE) to determine the baseline λ_{res} and its thermal sensitivity ($\partial\lambda_{res}/\partial T$). With the temperature profile defined, MODE is used to extract the effective index (n_{eff}) and group index (n_g) of the waveguide cross-section, while a Finite-Difference Time-Domain (FDTD) solver is utilized to extract r and k of the directional coupler region. These extracted parameters serve a dual purpose: they are used analytically to calculate the static optical transmission spectrum, and they are imported into INTERCONNECT to define the physical behavior of the MRR compound for subsequent system-level BER analysis.

Figure.5 MRR Simulation Flow

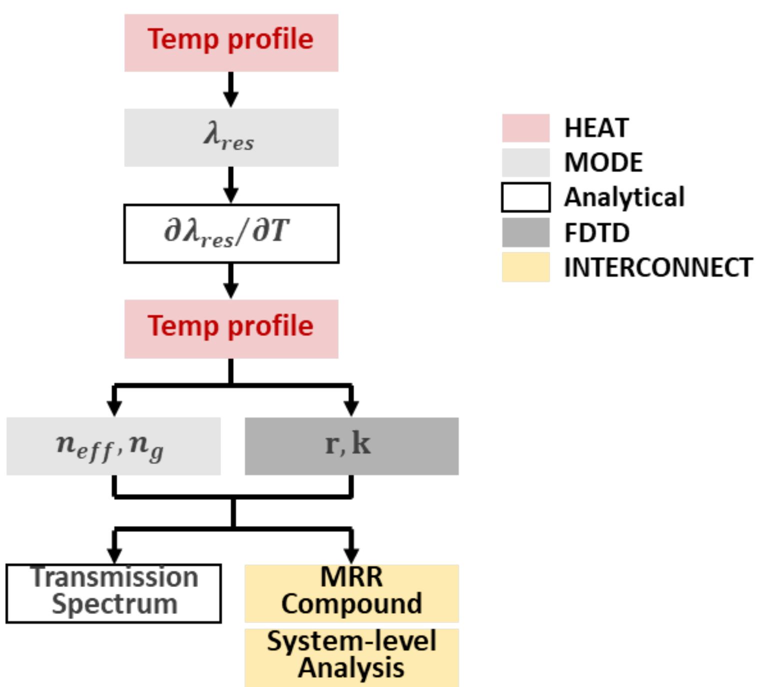

1. Solver Configurations – Lumerical MODE

Accurate extraction of waveguide parameters requires rigorous convergence testing and precise configuration of the simulation environment. For the FDE solver within Lumerical MODE, the dimensions of the simulation window and the structural definitions are critical to avoiding non-physical artifacts, particularly concerning propagation loss. If the window is too small, the evanescent tails of the optical mode will artificially overlap with the simulation boundaries, leading to an inaccurate, artificially reduced calculation of the waveguide loss. Conversely, for a curved waveguide structure like an MRR, the radial width of the simulation window cannot arbitrarily increase and is strictly upper bounded by the ring's radius itself to maintain physical validity in the cylindrical coordinate transformation.

Furthermore, the treatment of the silicon slab is critical when applying Perfectly Matched Layer (PML) absorbing boundaries. If the physical width of the slab is defined as finite and falls within the solver window, the PML boundaries will improperly interact with the scattering field components generated at the abrupt edges of the slab. This scattering causes the PML to fail, artificially inflating the loss—sometimes yielding non-physical positive gain/loss anomalies. Therefore, to ensure stability and accuracy, the simulated structure must be defined with an effectively infinite slab width that extends continuously through the PML boundaries.

2. Iterative Calculation of Resonance Wavelength

A fundamental step in the simulation flow is establishing the exact resonance wavelength of the unloaded MRR cavity. According to the round-trip phase condition, the resonance wavelength is defined by the equation: $\lambda_{res} = n_{eff}L/m$ where L is the physical round-trip length of the cavity and m is the azimuthal mode number, which must strictly be an integer for constructive interference to occur. However, calculating this analytically presents a circular dependency. n_{eff} is inherently highly dispersive, meaning it is a continuous function of the wavelength itself. Because m is restricted to discrete integer values, one cannot simply calculate n_{eff} at an arbitrary wavelength and directly solve for n_{eff}. To find the true physical resonance, an iterative numerical approach is required using the MODE solver. An initial wavelength estimate is provided to the FDE solver to calculate an initial n_{eff}. This value is then substituted back into the resonance equation to evaluate m. The wavelength is subsequently adjusted and fed back into the MODE solver iteratively until the product of the simulated n_{eff} and L perfectly satisfies the integer m condition, thereby locking in the precise λ_{res}

3. Solver Configuration – Lumerical FDTD

To characterize the directional coupling region between the straight bus waveguide and the curved ring waveguide, a 3D FDTD simulation is utilized. The primary objective of this simulation is to accurately extract $r(\lambda)$ and $k(\lambda)$ for the fundamental Transverse Electric (TE) mode. To achieve this with high modal purity, Lumerical "port" objects are implemented at the input and output boundaries of the simulation window. The use of port objects is strictly preferred over the conventional combination of a standard "mode source" and a spatial "monitor." Port objects automatically perform mode expansion, allowing the solver to inject a pure fundamental TE mode and explicitly extract the S-parameters, filtering out any scattered radiation or higher-order mode conversions that occur within the coupling region. The physical geometry constructed within the FDTD simulation window consists of a straight bus waveguide and a half-ring structure, as illustrated in the Figure.6 (top). Because a half-ring is used, the simulation inherently captures the excess radiation loss associated with modal propagation through a curved waveguide. However, this incorporated bend loss only affects the absolute transmission magnitude through the arc; it does not compromise the accurate extraction of the localized r at the bus-to-ring interaction gap. Since the raw S-parameter data extracted from the FDTD simulation reveals that the system is nearly lossless, as shown in Figure.6 (bot), the coupler loss is ignored in the rest of this thesis. Hence, the extracted r is taken as the ground truth, and k is subsequently calculated from $r^2 + k^2 = 1$.

Figure.6 FDTD configuration. (top) Screenshot of xy view in FDTD and (bot) Plot of simulated $\boldsymbol{a}$ (from MODE), $\boldsymbol{r}$, and $\boldsymbol{r^2} + \boldsymbol{k^2}$ for MRR#1.

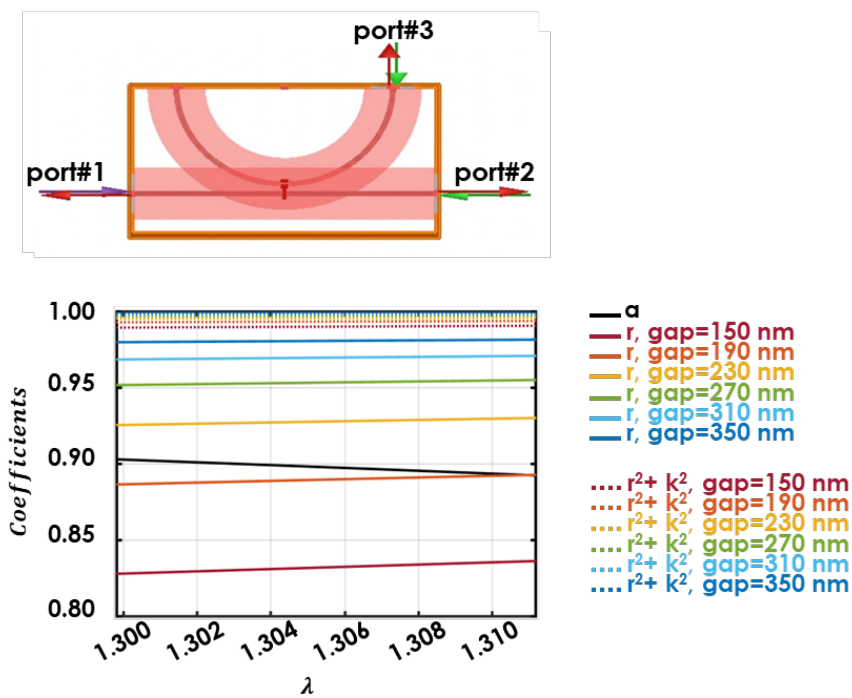

4. Solver Configurations – Lumerical HEAT

Conventionally, a 2D thermal simulation of the waveguide cross-section is utilized to calculate the temperature profile of a heated microring. However, this simplified approach can yield erroneous results when applied to the highly compact ring geometries required for high-speed applications. The fundamental flaw lies in the boundary conditions of a 2D configuration. The horizontal boundaries of the 2D simulation window must be defined as either "open" (representing an infinite, continuous expanse of oxide) or "closed" (representing a perfectly thermally insulated wall). Neither assumption physically represents the real, confined geometry of an MRR., because, in a physical MRR, the inner oxide region is completely enclosed by the active silicon ring and its integrated thermal heater. This geometry traps heat within the center of the ring, significantly elevating the overall temperature of the inner oxide core. This trapped heat conductively back-acts on the silicon, fundamentally altering the baseline temperature profile of the ring itself.

Furthermore, the conventional 2D cross-section ignores the thermal impact on the directional coupler. In modern high-speed MRMs, the gap between the ring and the straight bus waveguide is extremely narrow—typically less than 400 nm. Because of this extreme proximity, the thermal gradient induced by the ring's heater extends deeply into the bus waveguide, creating an asymmetric thermal perturbation across the entire coupling region.

To accurately capture these complex thermal dynamics, a complete 3D configuration is constructed using the Lumerical HEAT solver. By simulating the entire physical volume of the device, the thermal trapping within the inner oxide and the asymmetric thermal gradients across the narrow coupling gap are strictly preserved. From this comprehensive 3D thermal model, two distinct data sets are extracted to feed the subsequent optical solvers (MODE, FDTD).

5. Solver Configurations – Lumerical INTERCONNECT

To evaluate the system-level performance of the designed microring resonators, a 4-channel WDM link is constructed within Lumerical INTERCONNECT. This schematic integrates the component-level parameters—such as effective index, group index, and coupling coefficients extracted from the MODE, FDTD, and HEAT solvers—into a unified MRR compound model to perform dynamic time-domain simulations and evaluate the pre-FEC BER.

To establish a realistic but strictly controlled baseline for signal degradation, the simulation incorporates exactly two fundamental noise sources. First, Laser Relative Intensity Noise (RIN) is included to account for optical signal-dependent noise originating from the CW source. Second, thermal noise density at the receiver's photodetector (PD) is incorporated to represent optical signal-independent electrical noise. Because the primary objective of this project is to establish a rigorous device-to-system modeling methodology and isolate the performance of the MRR itself, other noise and loss mechanisms are intentionally excluded such as PD shot noise, driver jitter noise, fiber-to-chip coupling losses, and parasitic facet reflections.

Furthermore, the transmitter block in this simulation relies on an ideal amplitude modulator rather than a physically modeled MRM. This design choice is critical for isolating Rx MRR's filtering performance from any modulator-induced constraints, such as finite electro-optic bandwidth or transient chirp. It is acknowledged that utilizing an ideal, lossless transmitter might somewhat suppress the system-level impact of the Rx MRR's insertion loss; in a real WDM link, a physical MRM would inherently attenuate the optical power before it ever reaches Rx. Therefore, this modeling flow can be repeated by substituting the ideal modulator with a fully characterized MRM model in a complete transceiver design process.

Figure.7 INTERCONNECT configuration for 4ch MRR WDM filters

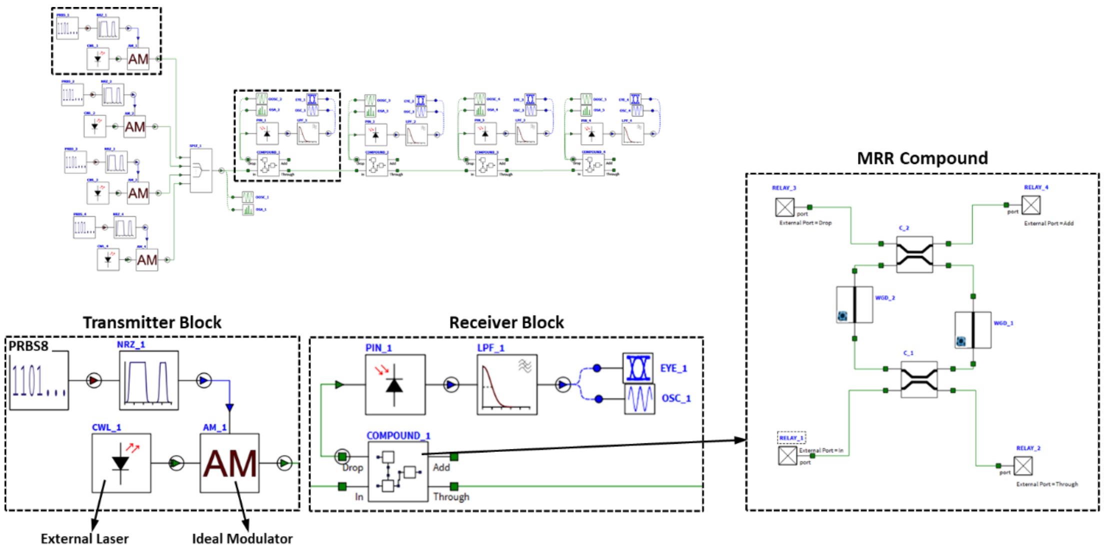

C. Transmission Spectrum

To validate the theoretical trade-offs established by the round-trip field model, the analytical transmission spectrum of MRR#1 ($a \approx 0.9$, comprising a 90 nm slab thickness and 7.5 μm R) was initially evaluated. As shown in the Figure.8, the simulated cavity yields 9.6 nm FSR. For a 4-channel WDM system, this dictates a channel spacing of 2.4 nm, which closely aligns with the standard OSI-MSA channel spacing of 2.3 nm [13].

By sweeping the coupling gap from 150 nm to 350 nm, the simulation clearly verifies the anticipated physical trade-offs: decreasing the gap (which reduces r) successfully increases the optical bandwidth, but at the direct expense of increased drop-port insertion loss and a reduced extinction ratio. Furthermore, analyzing the transmission spectrum of the cascaded 4-

channel architecture reveals that the individual channel outputs are distinctively different from one another, anticipating performance variations across the link: (1) crosstalk with the preceding channel is generally minimal, (2) crosstalk with the subsequent channel can be critical due to the overlap of the resonance tails, and (3) optical insertion loss accumulates sequentially across the bus waveguide, as shown in Figure.9. The CW light destined for the last channel must pass through the off-resonance cavities of all preceding channels, suffering parasitic scattering and absorption at each stage. Consequently, crosstalk strength is most severe in the middle channels (Ch2 ≈ Ch3 > Ch1 > Ch4), and insertion loss strictly penalizes the earlier channels in the drop sequence (Ch1 > Ch2 > Ch3 > Ch4).

Figure.8 4ch Individual Transmission Spectrum – MRR#1

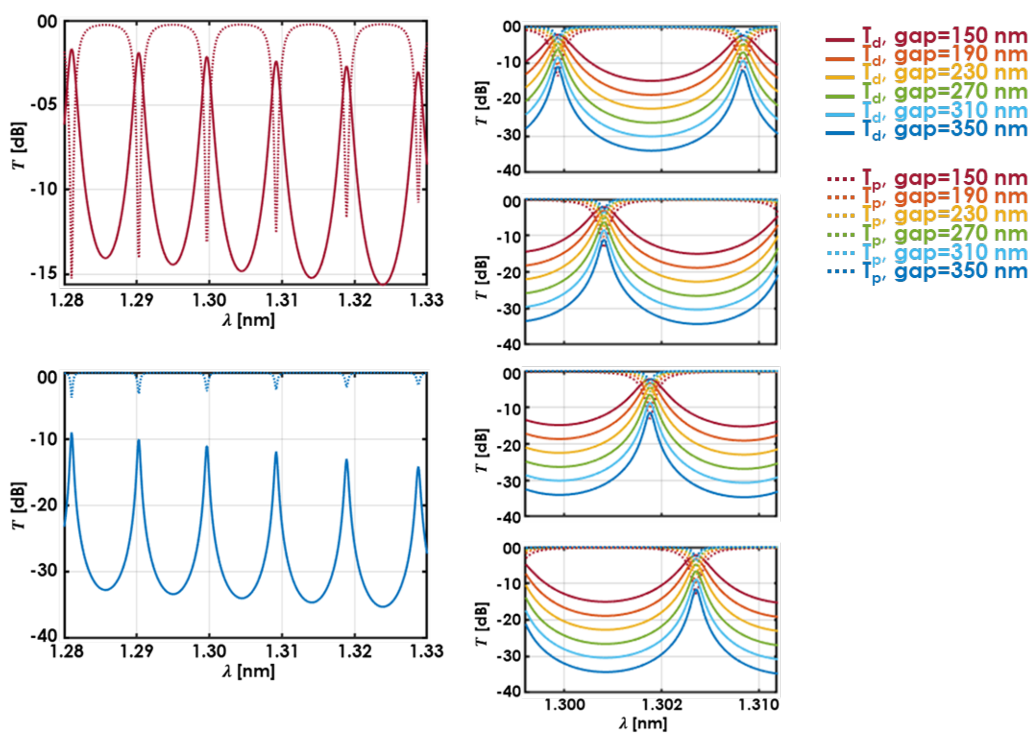

Figure.9 4ch Transmission Spectrum – MRR#1

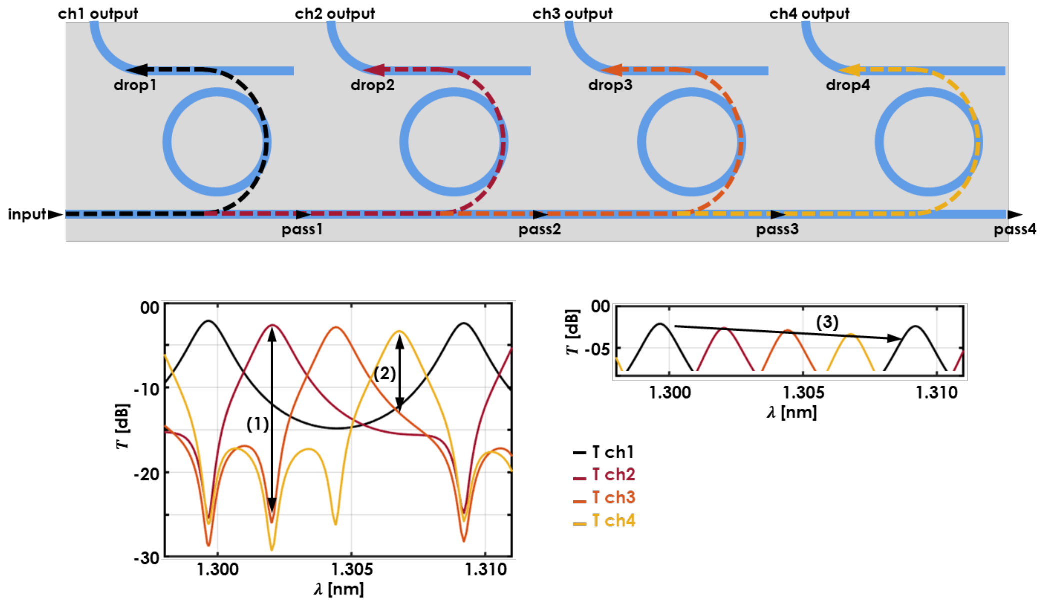

D. MRR Compound Characterization

1. Steady-state Transmission Spectrum

To accurately validate the constructed MRR compound model within Lumerical INTERCONNECT, a rigorous two-step characterization process is performed: a steady-state spectral analysis and a transient step-response analysis. For the initial steady-state characterization, an optical network analyzer element is utilized to continuously monitor the optical transmission at the channel outputs of the cascaded 4-channel MRR WDM filters as shown in Figure.10.

Figure.10 MRR compound steady-state characterization setup

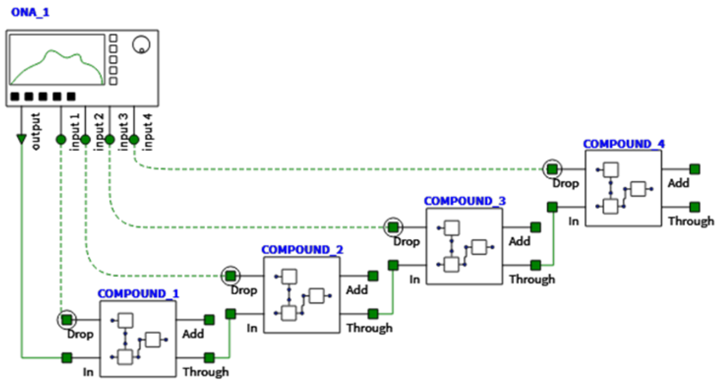

The resulting simulated transmission spectrum of the INTERCONNECT compound model is confirmed to be nearly identical to the analytically calculated spectrum, Figure.11. This precise alignment successfully validates that the parameters from device-level solvers are accurately mapped into the system-level environment.

Figure.11 MRR compound transmission spectrum

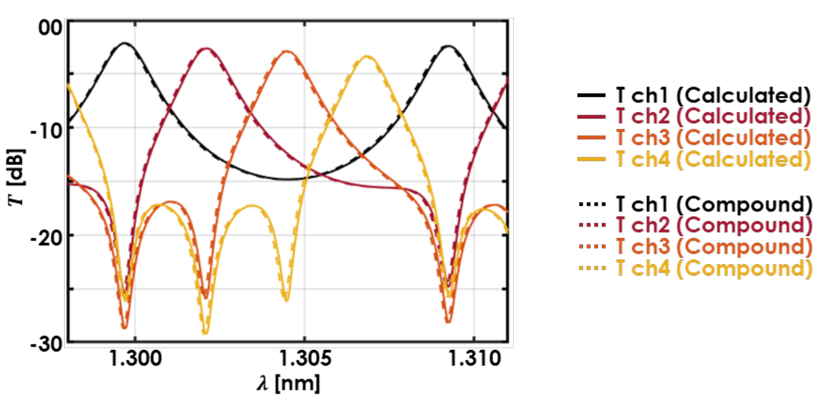

2. Transient step-response and effective 3dB bandwidth

Following the static validation, the dynamic transient behavior of the MRR compound is evaluated to extract its effective 3 dB bandwidth. This characterization is achieved by stimulating the model with a step source coupled to an ideal amplitude modulator, as shown in the simulation setup, shown in Figure.12. To ensure clear signal monitoring and eliminate stochastic interference, the laser RIN is intentionally disabled during this step.

Figure.12 MRR compound transient characterization setup

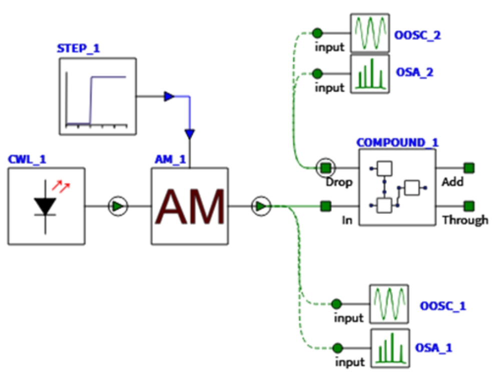

The resulting time-domain optical step response at the drop port is subsequently transformed into the frequency domain using a Fast Fourier Transform (FFT) to accurately isolate the 3 dB cut-off frequency (f_{3dB}). Evaluating these frequency-domain results reveals a strong simulation dependency on the chosen sample rate, shown in Figure.13. Applying a higher sample rate gradually increases the simulated 3 dB bandwidth until it eventually converges to its true physical value. However, pushing the sample rate higher significantly escalates the required simulation time. Because the primary objective of this thesis is to establish an end-to-end design flow and conduct extensive multi-parameter sweeps, the sample rate is fixed at 30 THz. This value is strategically selected to maintain acceptable numerical accuracy while preserving computational efficiency.

Figure.13 MRR's sample rate dependent transient response. MRR#1 (gap 150nm)

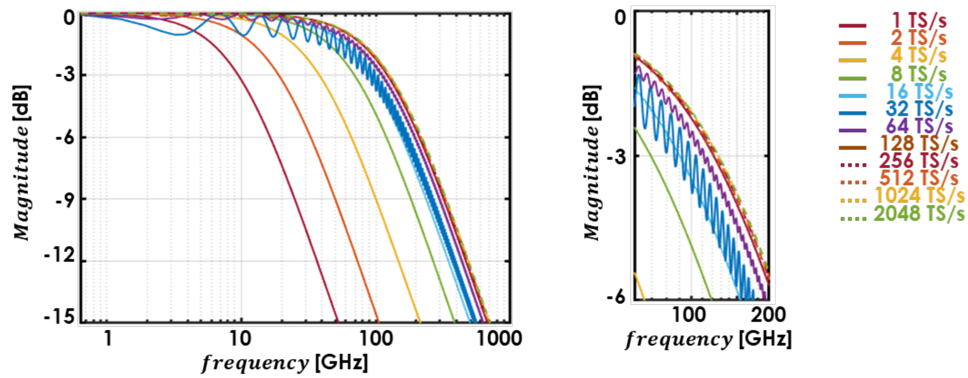

Analyzing the time-domain step response, Figure.14 provides direct validation of the optical power constraints. As the coupling gap increases both the absolute optical signal level and the Optical Modulation Amplitude (OMA) systematically decrease. This observed behavior in the dynamic compound model precisely confirms the insertion loss and extinction ratio trade-offs previously established by the theoretical round-trip model.

The frequency-domain FFT results, shown in Figure.15, further validate the theoretical cavity dynamics. The extracted data demonstrates that the f_{3dB} strictly decreases as the coupling gap increases, perfectly aligning with the photon lifetime limitations and bandwidth trade-offs discussed in the round-trip model section. Crucially, this transient step-response characterization definitively shows that the actual f_{3dB} observed at the drop port is nearly half of the analytically calculated f_{photon}. Although the physical MRR conceptually operates as an optical bandpass filter centered at its resonance wavelength, from the perspective of the demodulated baseband data signal, the optical cavity behaves entirely as an low-pass (LP) filter. This inherent low-pass characteristic dictates the device's transient response limit and acts as the primary mechanism inducing Inter-Symbol Interference (ISI) during high-speed data transmission.

Figure.14 MRR compound step-response in optical power. MRR#1 drop-port (top) output (bot) normalized output in response of input power 1mW and step trigger at 1 ns

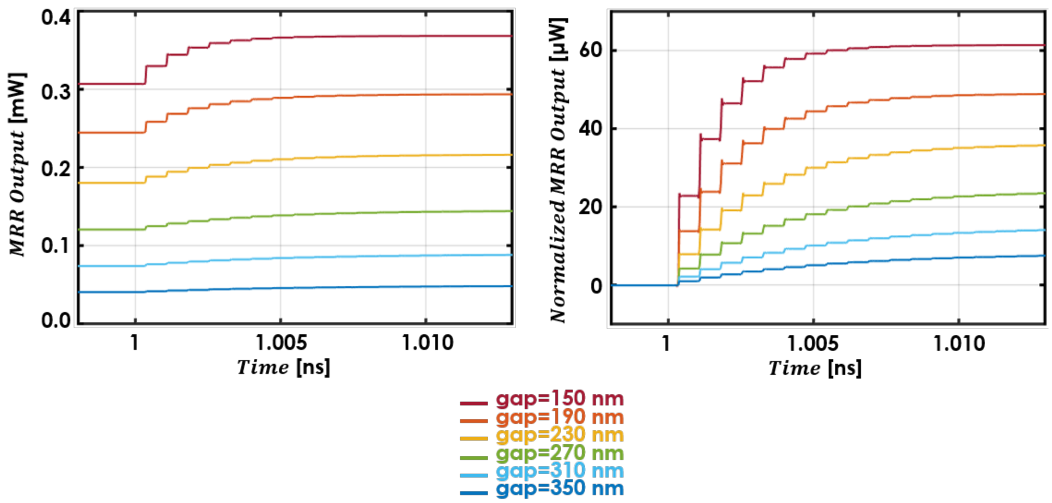

Figure.15 MRR compound step-response FFT results. MRR#1 drop-port (left) Magnitude (right) simulated f_{3dB} Vs calculated f_{photon}

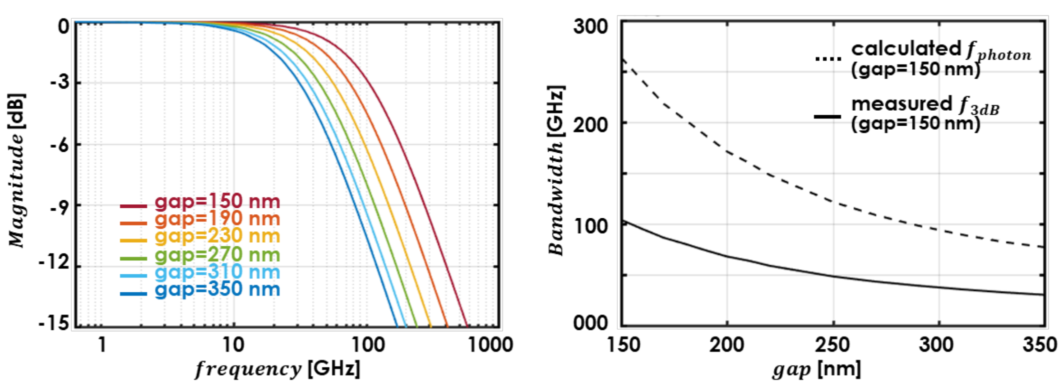

E. INTERCONNECT System-Level Results

Based on the INTERCONNECT configurations discussed earlier in Chapter#2-5, the system-level performance of the three varied MRR designs is evaluated by extracting the pre-FEC BER across a broad sweep of bitrates (50 GHz to 300 GHz) with 30 THz sample rate and 256 sequence length. The noise sources are laser RIN $-150\ dB/Hz$ [13] and Rx noise density $10\ pA/\sqrt{Hz}$ [41-43]. The BER is based on the Q method, calculated from the simulated one/zero level mean (μ) and sigma (σ), whose exact equation is as follows:

$$BER = \frac{1}{2} erfc\left(\frac{\mu_1 - \mu_0}{\sqrt{2}(\sigma_1 + \sigma_0)}\right)$$

As shown in Figure.16, the results reveal a clear performance inversion dependent on the operating speed. At moderate speeds (<100 Gbps), MRRs with a higher a, which possess lower IL_d and higher ER_d but narrower bandwidths, exhibit better BER performance. At these lower speeds, ISI is minimal, and the system is primarily power-constrained, making insertion loss the dominant penalty factor. At high speeds (>100 Gbps), conversely, MRRs with a lower a (such as MRR#1) demonstrate superior BER. As the baud rate increases, the transient response of the MRR cavity becomes the primary bottleneck. The wider optical bandwidth of the lower a design effectively mitigates ISI, overriding the penalty of its higher insertion loss. As the bitrate approaches the 200G/lane threshold, all evaluated MRR designs move near or eventually cross the pre-FEC limit dictated by concatenated FEC schemes. Therefore, prioritizing optical bandwidth to combat ISI, MRR#1 is chosen as the optimal baseline geometry for future high-speed link development for now.

When interpreting these results, it is crucial to account for the constraints of the simulation setup. Because an ideal modulator is utilized—effectively delivering an infinite Optical

Modulation Amplitude (OMA) with perfect zero (-100 dBm) and one (0 dBm) levels—the observed BER degradation is entirely dominated by the MRR's transient response (f_{photon}) rather than absolute optical power limitations (IL and ER). In a physical, fully integrated WDM link, a real silicon modulator will have a finite OMA, transient chirp, and intrinsic insertion loss, which will drastically compress the available power budget. Besides the ideal modulator used in the setup, becuase the sequence length is only 256 (bits), therefore, strictly speaking, ISI is not fully addressed. Consequently, a physical system with a proper number of bits (e.g. PRBS13 [13]) will require a significantly larger BER margin from Rx MRR.

Figure.16 4ch MRR WDM filter results. (left) simulated BER for different MRR models across 4 channels and (right) focused view of the high-speed range

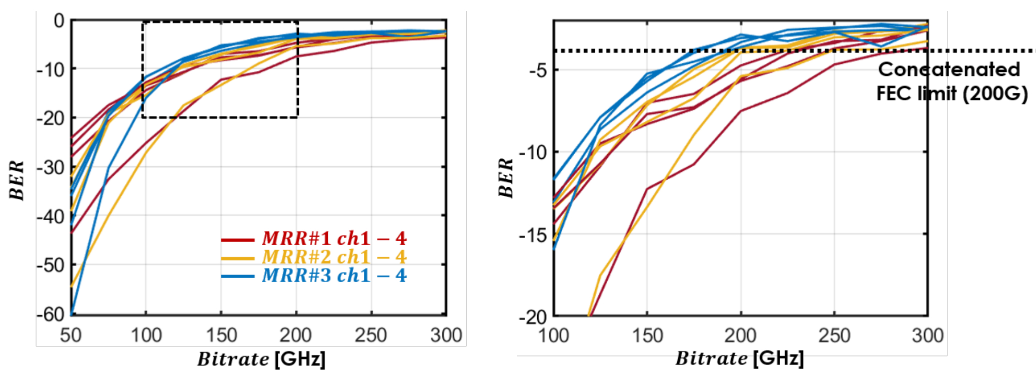

III. Microring Modulator

The fundamental operation of MRM is governed by the same round-trip field model established for the resonator. However, while the resonator performance is evaluated at the drop port, MRM is analyzed based on the transmission at the pass (through) port. Consequently, the specific analytical influence of a and r shifts slightly. Despite this shift in focus to the pass port, the inherent physical trade-offs remain remarkably similar as shown in Figure.17. Because these competing metrics directly dictate the quality of the modulated optical eye, a comprehensive parameter sweep and a final system-level BER analysis are required, just as they were for the resonator.

Figure.17 Calculated Characteristic Parameters. (left) Photon-lifetime limited bandwidth and (right) insertion loss and extinction ratio for the pass port as functions of the coupling coefficient for different round-trip loss coefficient where $\boldsymbol{r_1 = r_2 = r}$

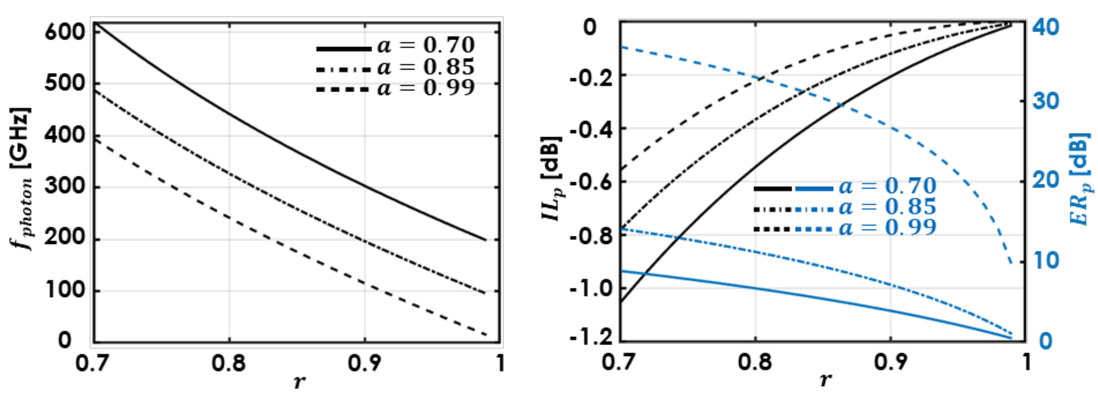

To maintain a controlled comparative baseline, the fundamental geometry of MRM—specifically the ring radius and waveguide widths—remains identical to the selected MRR#1. Hence, the baseline (undoped) f_{photon} is expected to be identical. However, an MRM requires the integration of a PN junction for active electro-optic modulation via the plasma dispersion effect [44,45]. Also, the introduction of dopants causes free-carrier absorption, which introduces additional propagation loss within the ring and the bus waveguide and subtly alters the round-trip transmission factor and coupling coefficients. This physical change dynamically alters every characteristic parameter, including optical bandwidth, insertion loss, and extinction ratio. Furthermore, the PN junction acts as an intrinsic electrical RC low-pass filter. Therefore, unlike a passive MRR where the transient response is solely dictated by the cavity photon lifetime, the total 3 dB bandwidth (f_{3dB}) of the MRM is a convolution of both the electrical RC bandwidth (f_{RC}) and the optical bandwidth (f_{photon}):

$$\frac{1}{{f_{3dB}}^2} = \frac{1}{{f_{RC}}^2} + \frac{1}{{f_{photon}}^2}$$

The magnitude of free-carrier dispersion and absorption is highly sensitive to the specific physical characteristics of the PN junction. These include the active doping concentration, the junction shape, its precise location relative to the optical mode, and the junction grading (e.g., the lateral scatter and vertical straggle resulting from the ion implantation process). Among these, junction grading is a strictly fabrication-induced parameter, rather than an arbitrary design variable that can be freely tuned in layout. Therefore, establishing the realistic and correct ranges and values of these parameters is critical for accurate predictive modelling. Usually, extracting these values requires comprehensive reference data, specifically the measured junction capacitance, the phase shift efficiency in pm/V, and the measured FWHM or f_{photon}. However, as discussed in the introductory chapter, the prevailing trend in silicon photonics literature focuses heavily on system-level device demonstrations, skipping underlying fabrication-level details.

A. Junction Parameter Benchmark

To overcome this lack of literature data and extract realistic junction parameters, reference data is benchmarked from the recent work of E. Chansky (UCSB, 2025) [35]. From his dissertation, a complete set of critical parameters is successfully extracted, including the junction capacitance, the phase shift efficiency, and the f_{photon}. This specific MRM, fabricated on the GF45CLO platform, was uniquely designed with a high doping level ($\sim 1 \times 10^{19}\ cm^{-3}$) to ensure device resilience under extreme radiation exposure [36]. To extract the specific junction grading parameters, a rigorous simulation sweep is conducted as shown in Figure.18.

Figure.18 Simulation flow and resultant loss functions for MRM junction parameter benchmark

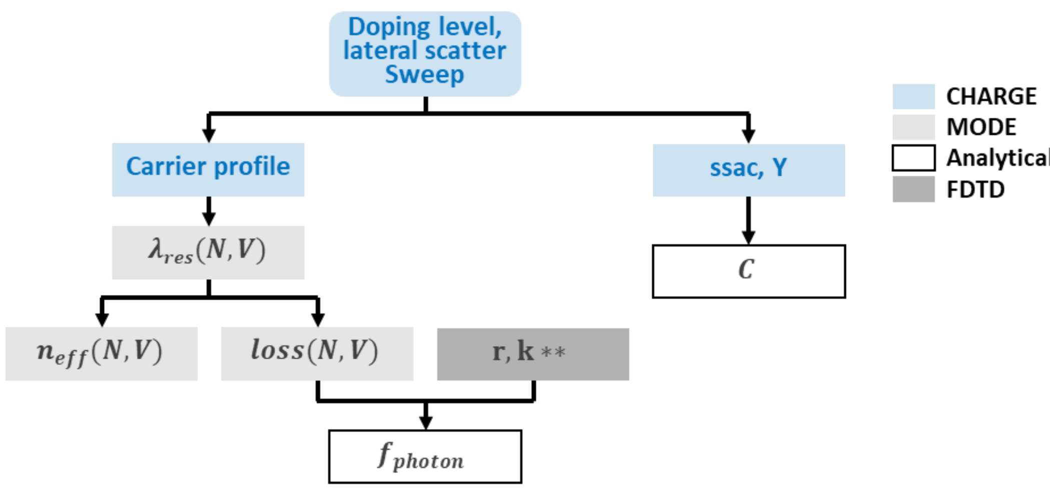

Assuming the doping profile is vertically uniform to simplify the problem, the active doping level is swept from 8×10^{18} to $1.4 \times 10^{19}\ cm^{-3}$ while the lateral scatter is swept from 5 to 30 nm. The later scatter sweep range is decided after literature reviews [46-47]. It must be noted that regardless of the established simulation flow, a directly coupled FDTD and

CHARGE simulation is technically unavailable due to the massive memory requirements. Therefore, undoped FDTD results are utilized to establish the baseline coupling parameters, while the active cavity shifts are strictly calculated using CHARGE and MODE solvers.

The optimal values are found using two distinct loss functions: one targeting the capacitance and the other targeting the phase shift. As shown in the corresponding heatmaps in Figure.19, both loss functions converge precisely on the same global minimum, successfully identifing the specific fabrication parameters of the reference device: a doping level of $1.3 \times 10^{19}\ cm^{-3}$ and a lateral scatter of 25 nm. With these critical fabrication uncertainties resolved, and the physical geometry matched to MRR#1, the foundational MRM model is fully defined and ready for high-speed device construction and simulation.

Figure.19 Loss functions for MRM junction parameter benchmark

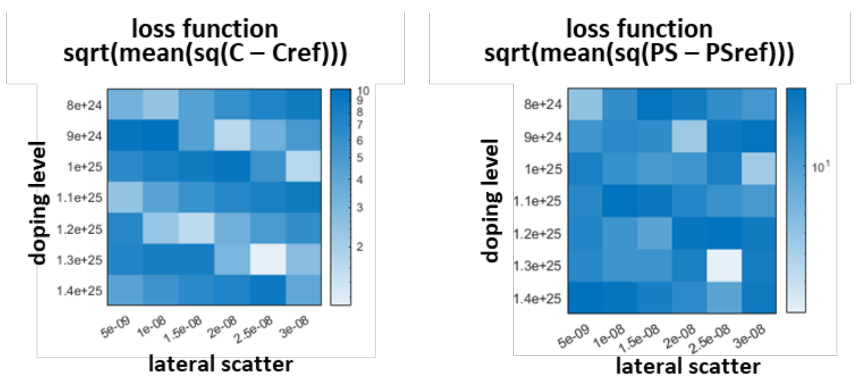

B. Investigation of Signal Level and OMA Requirements

Unlike the passive MRR filter, the transmitter MRM is an active device responsible for generating the modulated optical signal. Naively, one might assume that maximizing both the optical bandwidth and the applied peak-to-peak driving voltage (V_{pp}) would simultaneously yield a larger OMA and, consequently, better signal quality. However, these parameters cannot coexist optimally due to a fundamental physical trade-off. Achieving a high optical bandwidth inherently requires a wider FWHM according to the bandwidth equation we discussed earlier. A wider FWHM flattens the spectral slope of the resonance dip. As a result, applying the same V_{pp} voltage swing across a flatter slope produces a significantly smaller OMA. Furthermore, this fundamental bandwidth-OMA trade-off must be contextualized within the noise environment of the complete link. Because the WDM link is subject to both optical signal-dependent noise (laser RIN) and optical signal-independent noise (Rx thermal noise), the final signal quality is rather dependent on the signal average level (LEVEL), not purely determined by the absolute magnitude of the OMA. Since the intensity modulation takes place within the resonance dip of the MRM, the specific width ($FWHM$) and depth (ER) of that dip dictate both LEVEL and OMA of the transmitted signal. Therefore, it is expected that a specific optimal balance between LEVEL and OMA is required to overcome the noise floors. To systematically investigate this relationship, the system-level INTERCONNECT simulation is modified. The MRR filters are removed to isolate the transmitter's behavior, and the physical MRM is temporarily replaced by an ideal amplitude modulator to allow for independent control over the optical parameters, shown in Figure.20. The sample rate remains same, 30 THz, but the sequence length has increased to 8192 (13th order PRBS [13]) to fully comprehend ISI. Noise sources are RIN $-144\ dB/Hz$ [13] and Rx thermal noise density $10\ pA/\sqrt{Hz}$ [41-43].

Figure.20 INTERCONNECT setup for OMA requirement investigation

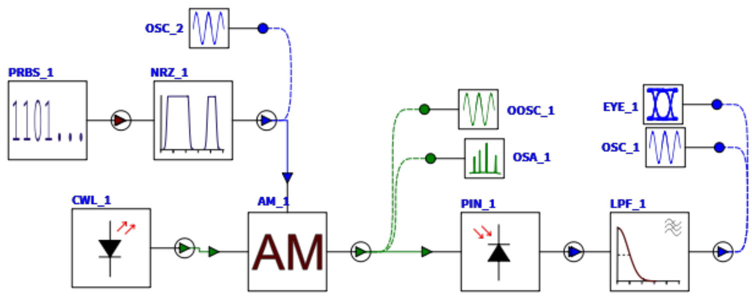

Exact values of Level and OMA are first calibrated with the system noise sources disabled to ensure strict accuracy. Subsequently, the noises are reactivated to simulate the resulting BER. The resulting heatmap as shown in Figure.21, evaluating the BER at 100 Gbps, clearly reveals a distinct performance trend: the system strongly benefits from operating at low LEVEL while maintaining a high OMA. Implementing this mathematically optimal condition (low LEVEL, high OMA) in a physical MRM presents significant engineering challenges. One potential method is to detune the CW laser wavelength closer to the center of the resonance, which naturally drops LEVEL. However, because the MRM's optical transfer function follows a Lorentzian shape, operating too close to the resonance severely compresses the achievable OMA. An alternative approach is to design the MRM cavity to have a higher ER with a much steeper resonance slope. Yet, as established previously in the round-trip model analysis, increasing the ER inherently penalizes the optical bandwidth. Because of these deeply intertwined, competing dynamics, the optimal design point cannot be found analytically. Thus, a comprehensive BER analysis utilizing parametric variations is strictly required to determine the true optimal operating conditions for the high-speed MRM.

Figure.21 BER at 100 Gbps with ideal amplitude modulator.

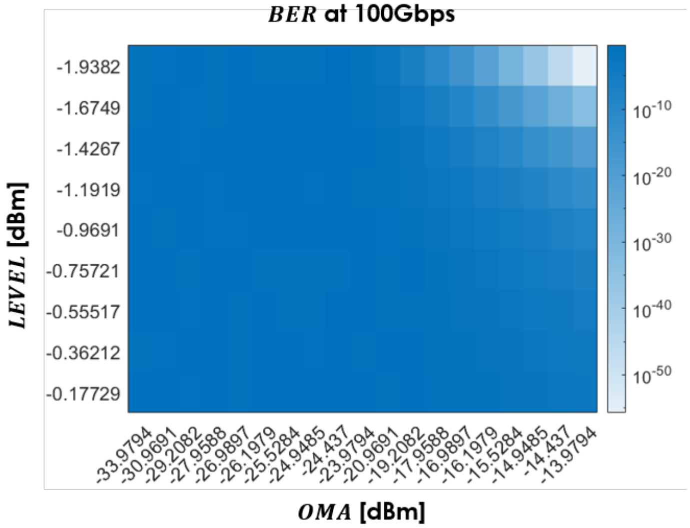

C. Simulation Flow and Bandwidth Factors

To systematically conduct the required BER analysis, a multi-dimensional parameter sweep is established. The selected sweep variables include the active doping level, the DC bias voltage, and V_{pp}. Variations in these parameters directly alter the free-carrier absorption within the waveguide, significantly changing the cavity loss and ultimately redefining MRM's optical transfer function. While the CW laser wavelength detuning is also a critical operational parameter, it is held constant, exactly at the wavelength that yields the maximum slope on the resonance dip, ensuring an optimal baseline for the OMA. Sweeping the detuning alongside the other three variables would expand the analysis into a highly complex 4D problem, which can be further explored in future works. The simulation flow is shown in Figure.22, fundamentally based on the Ansys examples [48-49].

Figure.22 Single MRM simulation flow

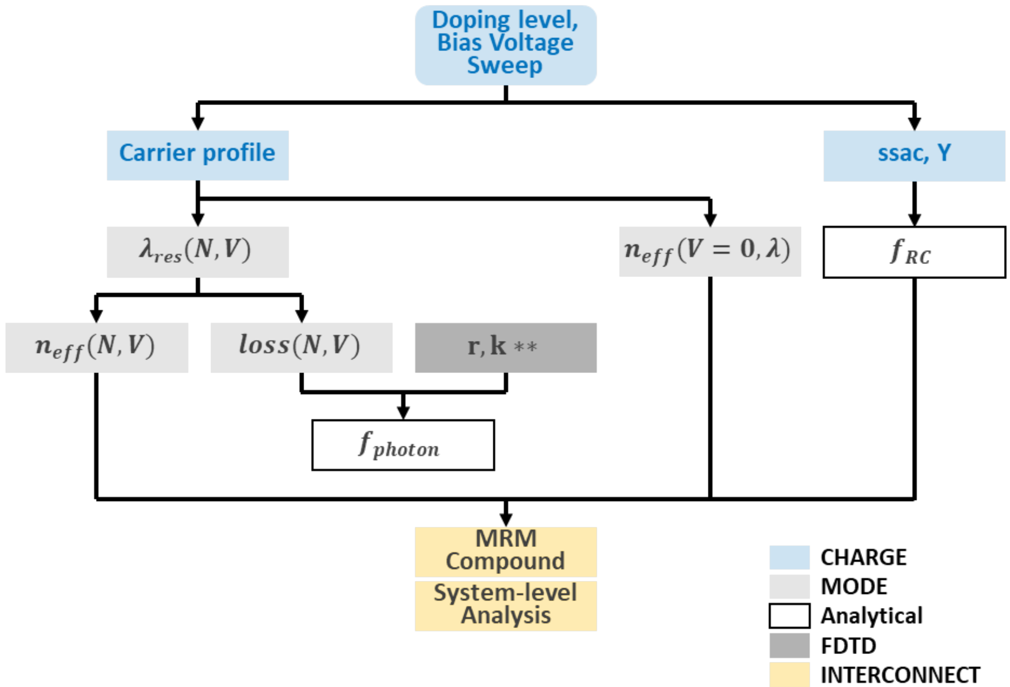

For every unique combination of doping and bias, the exact resonance point must first be searched and identified before the specific passive and active n_{eff} profiles are simulated and exported to the system-level model. Furthermore, this updated simulation flow explicitly incorporates the device's electrical RC response. By utilizing a small-signal AC (ssac) simulation within the CHARGE solver, the electrical admittance (Y) is evaluated to extract the precise junction series resistance and capacitance across all doping and bias variations, which determines the device intrinsic f_{RC}. The MRM compound model requires three distinct, independently simulated data sets: dispersion ($n_{eff}(N,V,\lambda)$), electro-optic efficiency ($n_{eff}(N,V,\lambda_{res})$), and coupling dynamics (r,k).

As illustrated in the resulting parametric heatmaps, Figure.23, the simulated f_{RC} is exceptionally high because all the extrinsic parasitic loads such as metal layers and packaging are excluded. Consequently, the total f_{3dB} is heavily dominated by f_{photon}. Nevertheless, a dedicated RC low-pass filter block is strictly integrated into the schematic, Figure.24.

Figure.23 Simulated RC and photon lifetime Bandwidth

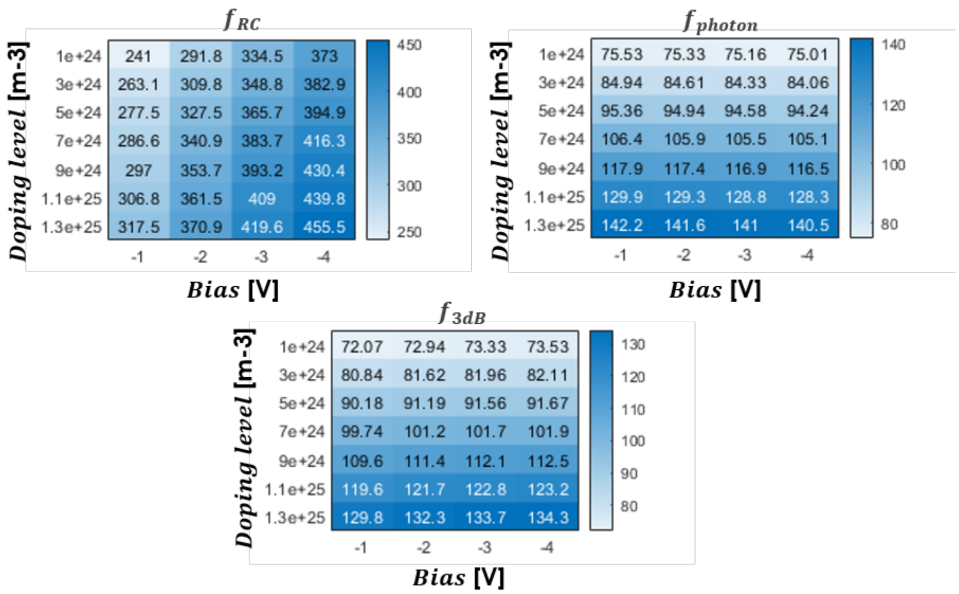

D. INTERCONNECT System-Level Results

The sample rate remains same, 30 THz, but the sequence length is increased to 8192 (13th order PRBS [13]) to fully comprehend ISI. Noise sources are RIN -144 dB/Hz [13] and Rx thermal noise density 10 pA/√Hz [41-43]. The system-level simulation results indicate that the optimal operating point for minimizing the BER does not strictly align with the bandwidth distribution discussed previously. This discrepancy underscores the critical necessity of comprehensive parameter sweeps rather than relying solely on analytical bandwidth maximization. Across all evaluated V_{pp}, a doping level of $5 \times 10^{18}\ cm^{-3}$ is consistently identified as the optimal value for BER performance. However, the required DC bias voltage shifts systematically as the driving voltage increases, requiring -2, -2, -3, and -4 V for $V_{pp} = 1,2,3,4$, respectively as shown in Figure.25.

Applying these optimized configurations, continuous bitrate sweeps are conducted to evaluate the ultimate high-speed limits of the device. The results demonstrate that at $V_{pp} = 2$, a 100 Gbps transmission rate is achievable while fully satisfying the concatenated FEC limit (RS(544, 514) + Hamming(128,120)). Achieving data rates beyond 100 Gbps, however, requires a significantly larger OMA. Even when driving the modulator aggressively at $V_{pp} = 4$, the device only marginally satisfies the concatenated FEC limit at 150 Gbps. Furthermore, if the stricter RS(544, 514) standard—commonly referred to as the HD-FEC limit—is applied, the maximum achievable bitrate decreases drastically across all simulated voltage configurations. From this comprehensive evaluation, navigating these complex trade-offs to pinpoint optimal operational parameters is crucial for high-speed MRM link design. The established correlation between higher V_{pp} and notably increased achievable bitrates suggests that advanced junction engineering, such as implementing vertical or Z-shaped PN junctions to maximize electro-optic overlap, will be highly beneficial for future designs [15,18,24,25]. Additionally, because signal quality was proven to be highly sensitive to the average optical power level within the resonance cavity, incorporating wavelength detuning as an additional sweep variable in future optimization cycles is expected to yield even further improvements in BER performance.

Figure.24 INTERCONNECT configuration for single MRM

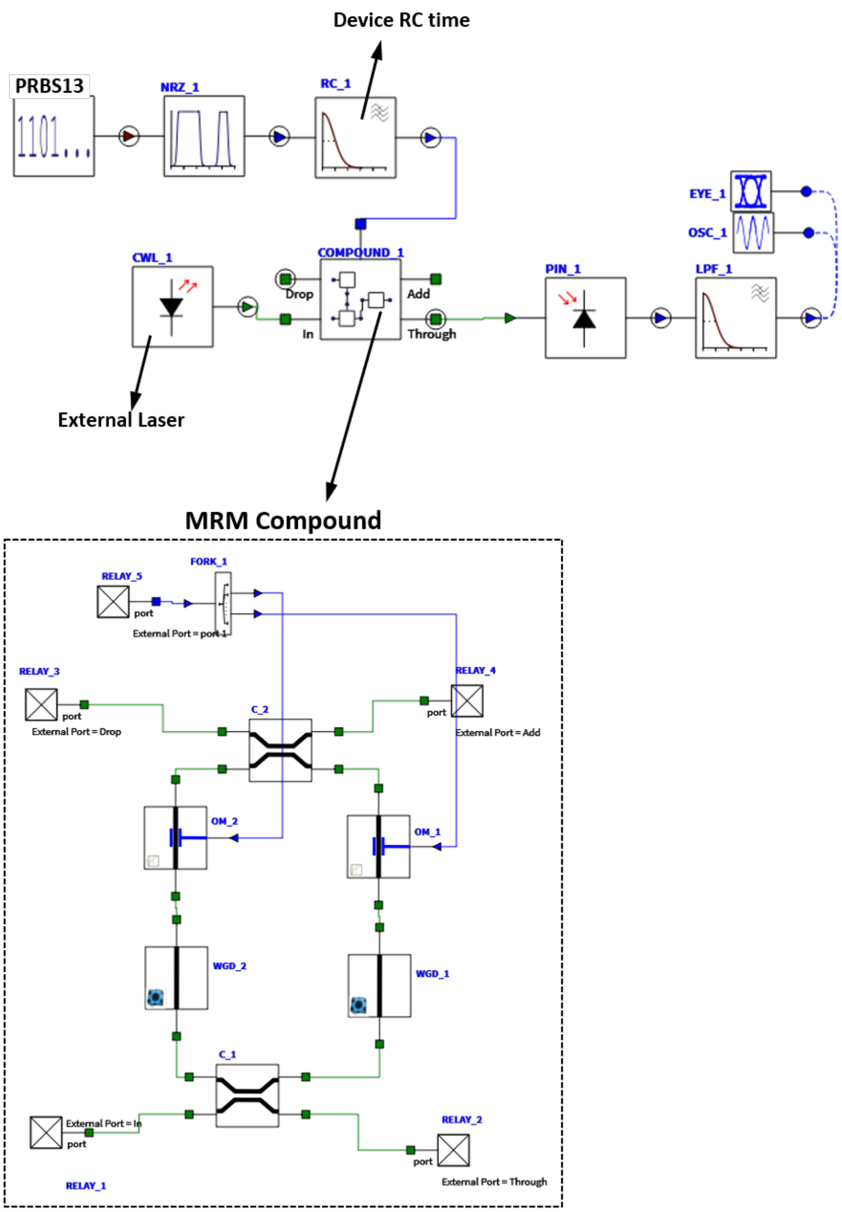

Figure.25 Single MRM results at 50 Gbps with different V_{pp}

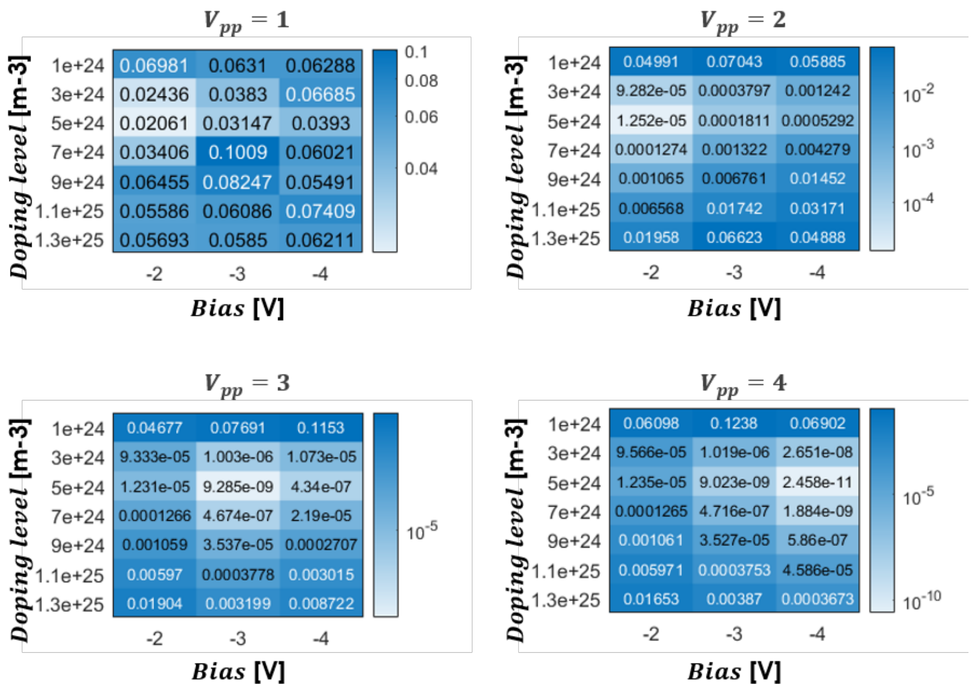

Figure.26 Single MRM results. Best cases for each V_{pp}. For all, doping level is $5 \times 10^{18}\ cm^{-3}$ The bias voltage is -2, -2, -3, -4 for $V_{pp} = 1,2,3,4$, respectively

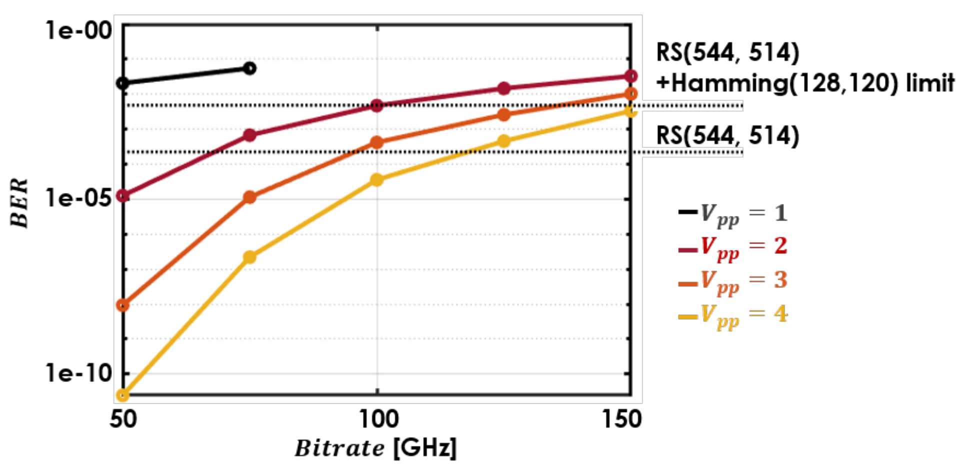

IV. Summary

A. Conclusion

This thesis successfully establishes and executes a rigorous device-to-system numerical modeling methodology to evaluate the high-speed performance limits of silicon MRM-MRR WDM links. By bridging the gap between component-level physical simulations and dynamic system-level evaluations, the complex and intertwining trade-offs inherent in MRM and MRR design are systematically quantified. The investigation into the passive Rx MRR explicitly demonstrates that at transmission speeds exceeding 100 Gbps, the transient low-pass behavior of the resonant cavity becomes the dominant performance bottleneck. Consequently, optimizing for a lower cavity Q-factor to widen the optical photon bandwidth is a strict necessity for mitigating Inter-Symbol Interference, even at the cost of elevated insertion loss and reduced extinction ratio.

Transitioning to the active transmitter MRM, the study confirms that achieving a sufficient OMA for high-speed signaling is severely constrained by the physical properties of the PN junction and the inherent Lorentzian shape of the optical transfer function. By benchmarking realistic fabrication variations and conducting multi-dimensional parameter sweeps across doping levels and bias voltages, the study successfully pinpoints an optimal device configuration. The resulting system-level BER analysis proves that while standard silicon MRMs can sustain 100 Gbps transmission under concatenated FEC limits with a moderate 2 V peak-to-peak driving voltage, pushing toward 150 Gbps and beyond yields rapidly diminishing returns.

Ultimately, this comprehensive numerical exploration serves a dual purpose. First, it provides a highly modular and robust simulation framework that can be directly applied to the future design of full MRM-MRR arrays and complete WDM transceiver links. Second, and perhaps more importantly, it analytically validates the presence of a rigid physical speed limit within standard silicon-on-insulator microring architectures. These findings substantiate the industry's accelerating shift toward advanced junction engineering and novel electro-optic platforms, providing a clear physical rationale for the next generation of photonic interconnect development.

B. Project Scope and Methodological Effort

The original ambition of this research was to design and construct a complete, fully characterized high-speed MRM-MRR WDM link. Bridging the gap from fundamental device physics to system-level evaluation is a massive undertaking, typically requiring a multi-year research timeline. The motivation for this work was identified following the 2024 IEEE International Electron Devices Meeting at San Fransico, CA, USA, where the critical bottleneck of AI data center interconnects highlighted a distinct research gap: a severe lack of comprehensive, system-level parametric studies for high-speed silicon microring WDM links.

To rigorously address this gap, the research timeline was strategically extended beyond standard degree requirements. The effort necessitated approximately six months dedicated to foundational physics and literature review, followed by nine months of extensive numerical simulation. Executing the multi-physics flow demanded several thousand individual simulations, equating to months of continuous computing time. To manage the high-density parameter sweeps, extensive automation scripts were developed from scratch. The process of writing, debugging, and refining these scripts ultimately required as much effort as configuring the physical device simulations. Furthermore, because the sheer computational load of the Lumerical software suite rapidly exceeded the capabilities of the shared server infrastructure at the university, dedicated high-performance computing resources were required to independently run the exhaustive trial-and-error cycles necessary to finalize the models.

Beyond the primary scientific findings, the comprehensive execution of this project cultivated significant technical competencies. Navigating the complex requirements of the simulation flow resulted in the development of advanced, industry-grade modeling skills across MODE, FDTD, HEAT, CHARGE, and INTERCONNECT. More broadly, the research demanded a highly practical, end-to-end understanding of the complete physics-to-device-to-system level design flow. These methodological capabilities not only fulfilled the immediate objectives of this thesis but also established a robust, scalable foundation for future photonic interconnect research.

C. Key Academic and Industry Takeaways

Beyond addressing the initial research gap, this project yields profound educational and professional insights that extend significantly beyond standard academic curricula. The rigorous execution of this methodology cultivated advanced, industry-grade simulation software skills and established a deep, practical understanding of the complete physics-to-device-to-system level design flow.

Crucially, the analysis of the final BER and transient response data leads to a stark realization: the active silicon MRM—and equally, the passive silicon MRR—possesses a rigid, fundamental physical speed limit. The inherent trade-offs among optical bandwidth, insertion loss, and extinction ratio create a hard ceiling for future baud rate scaling on standard silicon-on-insulator platforms. This technical conclusion aligns precisely with current industry trend. Observations from major recent photonics conferences (including Photonics West, OFC, and CLEO 2026) confirm that the industry's shift toward high-speed optical interconnects is accelerating significantly faster than previously anticipated. As explicitly stated by industry leaders at OFC 2026, the physical limits of standard silicon MRMs are now widely recognized, driving a strategic pivot toward novel, highly efficient electro-optic material platforms such as Thin-Film Lithium Niobate (TFLN) and Barium Titanate (BTO). Ultimately, this thesis underscores exactly why that material transition is fundamentally and physically necessary.

D. Future Work and Strategic Trajectory

While this thesis successfully established the simulation flow and characterized the baseline high-speed limits of individual MRM and MRR devices, the immediate future work required to realize the full WDM architecture includes:

- MRM Array Characterization: Expanding the single MRM model into a cascaded array to study transmitter-side inter-channel crosstalk and power penalties.
- Advanced Junction Engineering: Exploring novel PN junction topologies (e.g., vertical or Z-shaped junctions) to maximize electro-optic overlap and significantly improve the Optical Modulation Amplitude (OMA).
- Wavelength Detuning Optimization: Implementing continuous-wave laser detuning as an active sweep parameter to further optimize the delicate balance between average signal level and OMA for BER improvement.
- Complete WDM Link Characterization: Fusing the optimized MRM array and the Rx MRR filter bank into a unified system-level simulation.

Conventionally, the next academic steps for a silicon microring project would include a deep dive into thermal crosstalk mitigation, integrated heater design, and optical bi-stability limits. However, because this research has definitively exposed the rigid, uncompromising speed limits of standard silicon MRM-MRR links, expending further effort to optimize the complex behaviors of rings yields diminishing returns. Moving forward, the scientific and industrial community's efforts—and the methodologies developed within this thesis—would be far more beneficially applied to modeling and designing interconnects on emerging platforms like TFLN and BTO, where the fundamental bandwidth ceilings are vastly superior.

References

1. B. Khailany. “AI Accelerator Hardware and Research Directions” 2024 IEEE IEDM. Short Course 2: AI Systems and the Next Leap Forward. (2024).

2. Yeh, S. K., et al. “Silicon Photonics Platform for Next Generation Data Communication Technologies” 2024 IEEE IEDM. (2024): 1-4

3. Huang, Jensen. “GTC 2025 Keynote”. NVIDIA, 18 Mar. 2025 https://investor.nvidia.com/events-and-presentations/events-and-presentations/event-details/2025/GTC-2025-2025-piRb7Y2nU-/default.aspx

4. C. Sun et al. “TeraPHY: An O-Band WDM Electro-Optic Platform for Low Power, Terabit/s Optical I/O” 2020 IEEE Symposium on VLSI Technology. (2020): 1-2

5. S. Fathololoumi et al. “Highly Integrated 4 Tbps Silicon Photonic IC for Compute Fabric Connectivity” 2022 IEEE Symposium on High-Performance Interconnects (2022): 1-4

6. A. Geravand et al. “Ultrafast coherent dynamics of microring modulators” Nature Photonics 19 (2025): 740-750

7. Y. Wang et al. “Silicon Photonics Chip I/O for Ultra High-Bandwidth and Energy-Efficient Die-to-Die Connectivity” 2024 IEEE CICC (2024): 1-8

8. “IEEE 802.3df” IEEE, 03 Dec. 2022 https://standards.ieee.org/ieee/802.3df/11107/

9. X. He et al. "FEC architecture of B400GbE to support BER objective." IEEE 802.3 Beyond 400G Study Group (2021). https://www.ieee802.org/3/B400G/public/21_05/he_b400g_01_210426.pdf

10. S. Yin et al. "FEC Requirements for 800GbE/1.6 TbE Optics." IEEE 802.3df July Plenary Meeting. (2022). https://www.ieee802.org/3/df/public/22_07/yin_3df_01_2207.pdf

11. L. Patra et al. "Concatenated FEC proposal for 200G/Lane PMD." IEEE 802.3df May 2022 session (2022). https://www.ieee802.org/3/df/public/22_05/22_0518/patra_3df_01_220518.pdf

12. X. Zhou et al. "Next-Gen Datacenter and Campus Optics: Technology Choices beyond 200 Gbps per Lane IM-DD," Journal of Lightwave Technology 44(3). (2026): 845-860

13. D. Che and X. Chen. "Modulation Format and Digital Signal Processing for IM-DD Optics at Post-200G Era," Journal of Lightwave Technology 42(2). (2024): 588-605

14. W. Wang et al. "Real-Time FPGA Investigation of Potential FEC Schemes for 800G-ZR/ZR+ Forward Error Correction," Journal of Lightwave Technology 41(3) (2023): 926-933

15. "200G Optical Compute Interconnect Line Interface Specification" Version 1.0, OCI MSA, 10 Mar. 2026 https://oci-msa.org/assets/files/200G-OCI-Optical-Phy-Specification-v1.0.pdf

16. J. Chen et al. "Energy Efficient and High Bandwidth Quantum Dot Comb Laser Based Silicon Microring Transmitter for Optical Interconnects" IEEE Journal of Selected Topics in Quantum Electronics (2024): 1-11

17. H. Cai et al. "Lateral-Zigzag PN Junction Enabled High-Efficiency Silicon Micro-Ring Modulator Working at 100Gb/s" IEEE Photonics Technology Letters 34.10 (2022): 525-528

18. J. Xue et al. "A 64 Gbaud/s Hybrid-Integrated Optical Transmitter Based on a 60 GHz Silicon Photonic Dual-Segment Microring Modulator and a CMOS Driver for High-Bandwidth DWDM Optical I/O" Journal of Lightwave Technology 43.10 (2025): 4808-4818.

19. H. Li et al. "A 112 Gb/s PAM4 Silicon Photonics Transmitter With Microring Modulator and CMOS Driver" Journal of Lightwave Technology 38.1 (2020): 131-138.

20. J. Sun et al. "A 128 Gb/s PAM4 Silicon Microring Modulator With Integrated Thermo-Optic Resonance Tuning" Journal of Lightwave Technology 37.1 (2018): 110-115.

21. H. Cai et al. "Microcomb and Micro-Ring Modulator Driven DWDM Optical Transmitter With Ultra-High Speed of 20 × 128 Gb/s" Journal of Lightwave Technology 43.15 (2025): 7239-7245

22. F. Xu et al. "A High-Speed Silicon Ring Modulator with a Large Working Wavelength Range" Electronics (2079-9292) 13.15 (2024).

23. X. Wu et al. "Low-chirp push-pull dual-ring modulator with 144 Gb/s PAM-4 data transmission" Optics Express 28.18 (2020): 26492-26498.

24. M. Sakib et al. "A high-speed micro-ring modulator for next generation energy-efficient optical networks beyond 100 Gbaud" CLEO: Science and Innovations. 2021.

25. DWU. Chan et al. "Ultra-Wide Free-Spectral-Range Silicon Microring Modulator for High Capacity WDM" Journal of Lightwave Technology 40.24 (2022): 7848-

7855.

26. S. Zhao et al. “High modulation efficiency micro-ring modulator with low driving voltage for high speed optical interconnection” Optics Express 33.9 (2025): 19442-19452.

27. Y. Yuan et al. “A 5 × 200 Gbps microring modulator silicon chip empowered by two-segment Z-shape junctions” Nature Communications 15.1 (2024): 918.

28. DWU. Chan et al. “Sub-volt forward-biased silicon microring modulator at 210 Gb/s” Optics Letters 49.22 (2024): 6477-6480.

29. Y. Zhang et al. “240 Gb/s optical transmission based on an ultrafast silicon microring modulator” Photonics Research 10.4 (2022): 1127-1133.

30. J. Li et al. “Integrated silicon elliptical ring modulator with ultra-high bandwidth beyond 110 GHz” Optics Letters 50.18 (2025): 5857-5860.

31. J. Xue et al. “An 8×256 Gbps Silicon Photonic DWDM Transmitter with Thermally Stable Microring Modulators” 2025 OFC.

32. K. Lu et al. “Whispering Gallery Mode Enhanced Broadband and High-Speed Silicon Microring Modulator” Journal of Lightwave Technology 43.18 (2025): 8792-8798.

33. F. Hu et al. “300-Gbps optical interconnection using neural-network based silicon microring modulator” Communications Engineering 2.1 (2023): 67.

34. Ferraro, F. J., et al. "Imec silicon photonics platforms: performance overview and roadmap." Next-Generation Optical Communication: Components, Sub-Systems, and Systems XII. Vol. 12429. SPIE, 2023.

35. E. Chansky et al. “Silicon Photonic Modulators and Devices for Extreme Environment and Datacenter Links” University of California, Santa Barbara, PhD dissertation. (2025). https://escholarship.org/uc/item/2bd09917

36. E. Chansky et al. “Silicon Photonic Highly Doped Ring Modulators for Cryogenic & Radiation-Hard WDM Readout” CLEO: Applications and Technology. 2025.

37. W. Bogaerts et al. "Silicon microring resonators." Laser & photonics reviews 6.1 (2012): 47-73.

38. J. Heebner et al. “Optical microresonators: theory, fabrication, and applications” New York, NY: Springer New York (2008). https://doi.org/10.1007/978-0-387-73068-4

39. “Ring resonator getting started - Design and initial simulation” Ansys Optics, https://optics.ansys.com/hc/en-us/articles/360042800293-Ring-resonator-getting-started-Design-and-initial-simulation

40. “Ring resonator using INTERCONNECT primitive elements” Ansys Optics, https://optics.ansys.com/hc/en-us/articles/360042323794-Ring-resonator-using-INTERCONNECT-primitive-elements

41. S. Daneshgar et al. "A 128 Gb/s PAM4 Linear TIA with 12.6 pA/√Hz Noise Density in 22nm FinFET CMOS," 2021 IEEE RFIC. (2021): 135-138.

42. T.C. Hsueh et al. "Monolithic Silicon-Photonics Linear-Algebra Accelerators Enabling Next-Gen Massive MIMO," Journal of Lightwave Technology 42(22). (2024): 7903-7918.

43. J. Deng et al. "A 25Gbps Single-Ended to Differential Low-Noise Transimpedance Amplifier in 45nm SOI for High-Speed Optical Transceivers," IEEE TENCON 2024. (2024): 446-449.

44. R. Soref and B. Bennett, IEEE J. Quantum Electron. 23(1), 123-129, 1987

45. M. Nedeljkovic et al. "Free-Carrier Electrorefraction and Electroabsorption Modulation Predictions for Silicon Over the 1–14- μm Infrared Wavelength Range," IEEE Photonics Journal 3(6). (2011): 1171-1180

46. J. D. Plummer, M. D. Deal, and P. B. Griffin, “Ion Implantation in Silicon VLSI,” in Silicon VLSI Technology: Fundamentals, Practice, and Modeling. Upper Saddle River, NJ, USA: Prentice Hall, 2000

47. S. M. Sze and K. K. Ng, Physics of Semiconductor Devices, 3rd ed. Hoboken, NJ, USA: Wiley-Interscience, 2007

48. “Ring Modulator” Ansys Optics, https://optics.ansys.com/hc/en-us/articles/360042322794-Ring-Modulator

49. “Ring modulator time domain (INTERCONNECT)” Ansys Optics, https://optics.ansys.com/hc/en-us/articles/360042329094-Ring-modulator-time-domain-INTERCONNECT